Naval Research Laboratory
Stennis Space Center, MS 39529-5004

NRL/MR/7332--97-8067

Effect of Surface Tilting on Altimeter Wind Measurements

PAUL A. HWANG
WILLIAM J. TEAGUE
GREGG A. JACOBS

Ocean Sciences Branch
Oceanography Division

DAVID W. WANG

Computer Science Corporation
Stennis Space Center, MS

October 17, 1997

REPORT DOCUMENTATION PAGE

Form Approved
OBM No. 0704-0188

1. AGENCY USE ONLY *(Leave blank)*	2. REPORT DATE	3. REPORT TYPE AND DATES COVERED
	October 17, 1997	Final

4. TITLE AND SUBTITLE

Effect of Surface Tilting on Altimeter Wind Measurements

5. FUNDING NUMBERS

Job Order No. 573704607
Program Element No. 0603832D
Project No. DMSO-97-0117
Task No.
Accession No.

6. AUTHOR(S)

Paul A. Hwang, William J. Teague, Gregg A. Jacobs, and David W. Wang*

7. PERFORMING ORGANIZATION NAME(S) AND ADDRESS(ES)

Naval Research Laboratory
Oceanography Division
Stennis Space Center, MS 39529-5004

8. PERFORMING ORGANIZATION REPORT NUMBER

NRL/MR/7332--97-8067

9. SPONSORING/MONITORING AGENCY NAME(S) AND ADDRESS(ES)

Naval Research Laboratory
Oceanography Division
Stennis Space Center, MS 39529-5004

10. SPONSORING/MONITORING AGENCY REPORT NUMBER

11. SUPPLEMENTARY NOTES

*Computer Science Corporation, Stennis Space Center, MS 39529

12a. DISTRIBUTION/AVAILABILITY STATEMENT

Approved for public release; distribution unlimited

12b. DISTRIBUTION CODE

13. ABSTRACT *(Maximum 200 words)*

A two-scale surface roughness model is presented to interpret the backscattering of satellite radar altimeters. It is found that the tilting effect of long waves produces an attenuation of the radar backscatter cross section. The calculated attenuation factor is in excellent agreement with TOPEX/POSEIDON (referred to as TOPEX for brevity) measurements. Two major contributors to the tilting mechanism are the wind-generated waves with the wavelengths much longer than the radar wavelength, and the ambient waves generated elsewhere that propagate into the measurement region. Using the information of the wavenumber spectra of short capillary-gravity waves measured in the ocean and an estimate of the ambient tilting wave components from ocean buoy measurements, computations of the tilting mechanism are carried out. The calculated attenuation factor is in excellent agreement with TOPEX measurements. With the tilting effect accounted, the agreement improves significantly between the wind speeds derived from the TOPEX Ku-band altimeter and those from the collocated ocean buoys.

14. SUBJECT TERMS

altimeter, waves, wind, buoys, tilt effect, altimeter backscatter

15. NUMBER OF PAGES

20

16. PRICE CODE

17. SECURITY CLASSIFICATION OF REPORT	18. SECURITY CLASSIFICATION OF THIS PAGE	19. SECURITY CLASSIFICATION OF ABSTRACT	20. LIMITATION OF ABSTRACT
Unclassified	Unclassified	Unclassified	SAR

EFFECT OF SURFACE TILTING ON ALTIMETER WIND MEASUREMENTS

1. Introduction

Feasibility of deriving the sea surface wind speed from satellite altimeters has been convincingly demonstrated during the past two decades with output from GEOS, SEASAT, GEOSAT and most recently TOPEX/POSEIDON missions (e.g., Brown, 1978, 1990; Brown et al., 1981; Chelton and Wentz, 1986; Witter and Chelton, 1991; Wu, 1992; Ebuchi and Kawamura, 1994; Freilich and Challenor, 1994; Gower, 1996). The basis for relating radar measurements to wind speed is the realization that radar backscatter is caused by surface roughness. In the ocean, the surface roughness is mainly contributed by wind-generated surface waves. The measured radar intensity (the normalized radar cross section), σ_0, however, was found to differ significantly from theoretical calculations using equations derived from scattering processes (e.g., Barrick, 1968) and measured physical properties of the surface roughness (e.g., Cox and Munk, 1954; Hwang et al., 1996). Most puzzling of all, calculations consistently indicated that the sea surface detected by radars, with wavelengths on the order of a few centimeters, was "rougher" than those detected by optical instruments that depend on light with wavelengths in the sub-micrometer wavelength range (e.g., Brown, 1990; Jackson et al., 1992). This perplexing result was not resolved in the past two decades since the advent of altimeter data. Up to this stage, the majority of wind speed algorithms are based on empirical or statistical analyses. Some of these also incorporate the physics of scattering processes and roughness properties (e.g., Brown et al., 1981; Wu, 1992), but most of them rely on correlation of coincident and collocated databases of the satellite radar cross section and in-situ wind speed (e.g., Chelton and Wentz, 1986; Witter and Chelton, 1991). One algorithm (Freilich and Challenor, 1994) relies completely on the independently derived statistical properties of the altimeter backscattering cross section and sea surface wind speed. The difference among these algorithms are relatively minor, and it will be shown that the results of these comparisons are sensitive to the databases used for the studies.

In this paper, we investigate the relationship between the surface roughness and radar cross section. In particular, we quantify the attenuation of the radar cross section as a result of the tilting of scattering roughness by surface water waves with wavelengths much longer than that of the radar waves. Because wave scattering processes depend strongly on the length scales of the roughness (relative to the radar wavelength), the clarification of different scattering contributions by surface roughness components of different length scales is a critical step for the improvement of the wind speed derivation by satellite altimetry. At higher wind speed conditions, wave breaking may become a significant factor to the variation of radar backscattering. The issue of breaking waves is not discussed in this paper.

In Section 2, the scattering of radar waves at near normal incidence is discussed (Section 2.1). A comparison of the mean square slopes derived from the radar backscattering equation with the optical measurements is quantitatively described (Section 2.2). Based on this analysis, a mathematical formulation of the surface tilting effect on the radar backscatter at normal incidence is described (Section 2.3). It is shown that the characteristics of the solution is in agreement with the observed radar-optical discrepancies.

A detailed numerical computation of the tilting solution is then carried out in Section 3. The length scales for the partitioning of the roughness components is described (Section 3.1). The wavenumber spectrum recently obtained from the ocean using a scanning slope sensor buoy (Hwang et al., 1996; Hwang, 1997) is used to derive the wind-generated tilting and scattering roughness (Section 3.2). In addition to local wind-generated waves, ambient waves (such as swells that are not originated in the local regions or turbulence process that are not related to local wind conditions) may also contribute to the tilting surface slopes (Section 3.3). With these considerations, the roughness components can be

quantitatively specified for the computation of the tilting mechanism. The tilting effect can be evaluated in a forward or inverse procedure. The general properties of the tilting solution are discussed (Section 3.4).

Section 4 presents a comparison of the tilting algorithms with existing empirical operational algorithms. The present status of the existing algorithms is briefly reviewed (Section 4.1). Quantitative comparison of two computational procedures to evaluate the tilting mechanism are described (Section 4.2). From comparisons of three data sets, with maximum distance between the buoy station and satellite footprint 10, 20, and 40 km, it is illustrated convincingly that the consideration of tilting effect significantly improves the agreement of wind speed measurements from satellite altimeters and in-situ ocean buoys. The results suggest that the accuracy of the satellite altimeter for measuring the wind speed at the ocean surface is better than we have perceived. It is also pointed out that in order to retrieve the wind speed to the full potential of the altimeter accuracy, we need to derive the ambient and tilting wave slope components from the altimeter data suite (Section 4.3). Finally, Section 5 presents the summary and conclusions.

2. Radar Backscatter at Normal Incidence

2.1. Scattering equation

The topic of wave scattering from a surface or by particles has been studied in many different contexts, including research in optical, acoustic, radar and water waves. A common result of these studies is that the scattering characteristics are critically controlled by the length scales of the object and the incident waves, as well as the refractive index of the medium, m. The length scales can be expressed in dimensionless form as $x=\kappa a$, where κ is the wavenumber of incident waves, defined as $2\pi/\lambda$, λ is the incident wavelength, and a is a characteristic length scale of the scattering object. Extensive discussions on wave scattering are available in the literature (e.g. Beckmann and Spizzichino, 1963; Fock, 1965; van de Hulst, 1987; Stewart, 1985). Using scattering from particles as an example, for very small particles ($mx<<1$) the scattering cross section is proportional to a^6. Therefore, the scattering contribution from very small-scale roughness diminishes rapidly. For very large particles, the incident beam may be considered to consist of separate rays. The behavior of these rays becomes independent if the separation distance is on the order of one incident wavelength. For a given frequency of incident waves, as the length scale of the scatterers in the medium becomes longer, the scattering pattern becomes sharper and more localized (e.g., van de Hulst, 1987).

A conceptual sketch is shown in **Figure** 1 to describe the situation of radar waves scattering from an undulating surface with different roughness properties and the resulting intensity patterns of the scattered waves. The sketch illustrates a train of plane waves (indicated by the parallel wave front) impinging on the water surface, corresponding to the far-field radar waves from satellite altimeters. The scattered wave patterns from the water surface will vary according to the surface roughness conditions, been more directional and narrowly distributed from a smooth surface, as in patch 1. The primary direction of the scattering pattern is along the direction of specular reflection. Therefore, for surfaces of equivalent roughness, such as patches 2, 3 and 4, the scattering patterns are similar in the directional distribution (the beam width, determined by the surface roughness), but the primary direction of the scattering will vary depending on the orientation of the roughness patch. The backscattering intensities, that is, the scattering in the direction opposite to the incoming waves, for the three patches shown will be different. The modification results in a reduced, or attenuated, radar return compared to the condition when the scattering is assumed to be on a flat surface such as depicted in patch 5. The concept illustrated in **Figure** 1 forms the basis of this paper regarding the tilting effect on the altimeter scattering from the ocean surface.

For monostatic radar applications, that is, projecting and receiving radar waves with the same antenna, backscattering properties are of most interest. The backscattering intensity is generally

expressed as the normalized radar cross section (NRCS), σ_0. Many expressions of σ_0 have been presented in the literature (e.g., Kerr, 1981; Wright, 1966, 1968; Barrick, 1968; Valenzuela, 1978). The major differences of their results are the assumptions of the surface roughness and the dielectric constant of sea water, which determines the refractive index of the sea surface (Stogryn, 1971; Ray, 1972; Klein and Swift, 1977). For radar altimeter applications, the expression given in Barrick (1968), frequently employed as the starting point (assuming a Gaussian distribution of the scattering surface roughness), is

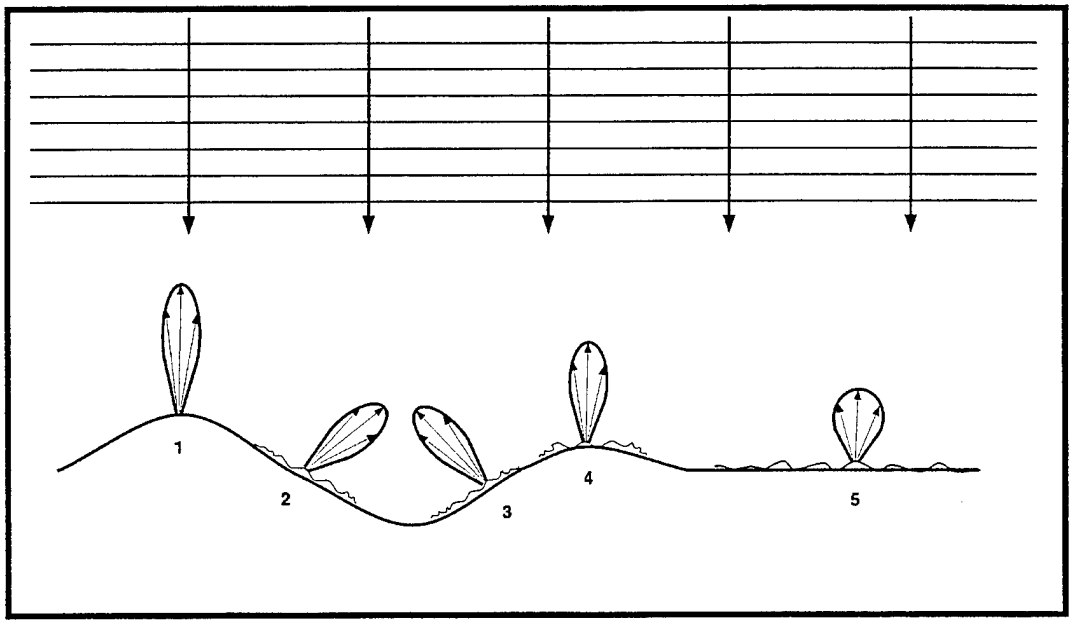

Figure 1. A conceptual sketch depicting the scattering of waves by surface roughness of various characteristics and the effect of tilting surface on the backscattering intensity from patches of similar roughness. See text for further description.

$$\sigma_o(\theta_i) = \frac{|R(0)|^2}{s_f^{\,2}} \sec^4 \theta_i \exp\left(\frac{-\tan^2 \theta_i}{s_f^{\,2}}\right), \qquad (1)$$

where θ_i is the radar incidence angle, denoting the angle between the propagation direction of radar waves and the surface normal; $|R(0)|^2$ is the Fresnel reflection coefficient, characterizing the surface reflectivity; and s_f^2 is the filtered mean square slope, representing the portion of surface roughness elements with length scales greater than the diffraction limit. Eq. (1) corresponds to the zero-th order solution of the scattering of electromagnetic waves from a rough surface (see also Brown, 1990; Jackson et al., 1992).

The wavelength of the diffraction limit, k_d, is generally specified to be scaled with the radar wavelength. The magnitude of the proportionality constant is not well defined, and Brown (1978, p. 479) states that "... there is very little theoretical foundation for choosing k_d other than $4k_0^2\zeta_s^2 << 1$." In this statement $k_0^2\zeta_s^2$ represents the mean square product of the electromagnetic wavenumber, k_0 (the equivalence of κ in this paper), and the surface roughness height, ζ_s, responsible for the scattering. For example, **Table** 2 of Jackson et al. (1992) lists the values cited in seven papers that range from 1.5 to 40. The most frequently used value is 3. It is noted that the calculation of roughness components requires the wavenumber spectral information of short waves in the size range of the radar wavelengths. Such information remains unknown to this date, although some spatial measurements of capillary-gravity

waves from the ocean started to appear in the literature (e.g., Hwang et al., 1996; Hwang, 1997 and the references therein). In any case, with a normal incidence, $\theta_i=0$, (1) can be expressed as

$$\sigma_o(0) = \frac{|R(0)|^2}{s_f^2} . \tag{2}$$

In the following, we shall write $\sigma_0=\sigma_0(0)$ for brevity.

2.2. Comparison of radar and optical measurements of mean square slopes

In the past, because of the relatively large footprint of the altimeter coverage (the footprint diameter of satellite altimeters is on the order of 7 km, see e.g., Chelton et al., 1989), all ocean waves with wavelengths greater than the diffraction limit of the radar waves were considered as the filtered roughness, s_f^2, in equation (2). The calculated roughness was significantly greater than physically possible, i.e., the calculated surface roughness appeared to be rougher for radar waves than for optical waves, as discussed in the last section. **Figure** 2a and 2b show the wind-speed dependence of mean square slopes measured by optical techniques (Cox and Munk, 1954; Hughes et al., 1978; Hwang, 1995, 1997; Hwang et al., 1996) and by microwave radars. A more thorough discussion of the available data sets of the optically-measured mean square slopes derived from the ocean environment is given in Hwang (1995, 1997). In **Figure** 2a, four measurements (shown as ⊕) at low-wind conditions (U_{10}<2 m/s) in the Cox and Munk (1954) data set are influenced by large swells present. The swell contribution ($(KH)^2/8$, where K and H are the wavenumber and wave height of the swells) can be calculated from the wave period and wave height reported (see Hwang, 1995, 1997 for more details). With this correction, all the optically-measured total mean square slopes, s^2, follow a clear trend of linear wind speed dependence. The least square fitting yields

$$s^2 = 5.12\times10^{-3}U_{10} + 1.25\times10^{-3} , \tag{3}$$

where U_{10} is the reference wind speed at a 10 m elevation. The scatter of these field data is within the factor-of-two envelope drawn as dashed curves in **Figure** 2a.

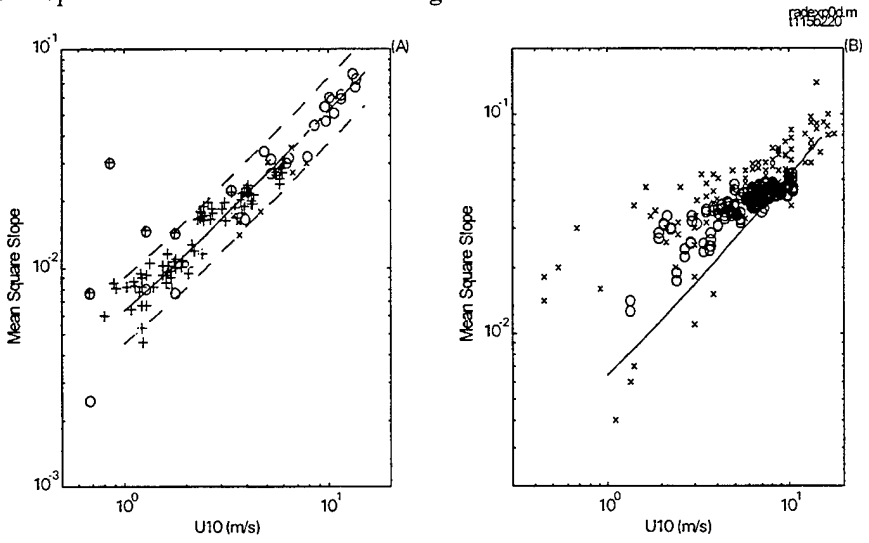

Figure 2. Comparison of mean square slopes derived from optical methods and satellite Ku-band altimeters. (a) Measurements using optical techniques, data shown are from: o: Cox and Munk (1954), the four data points plotted as ⊕ are without the correction of swell contribution (see text for further discussion); x: Hughes et al. (1978); and +: Hwang et al., (1996) and Hwang (1997). The solid curve is the linear best fit represented by Eq. (3); and the dashed curves are the factor-of-two envelopes (b) Measurements from GEOS-3 (×) and TOPEX (o) altimeters. The GEOS-3 data is digitized from figure 7 of Brown (1990), the TOPEX data is from Track 115 and NDBC data is from Buoy 42020 in the Gulf of Mexico. The solid curve is Eq. (3).

In contrast to the optical data, the dependence between wind speed and radar-derived surface roughness (using equation (2)) is more complicated (**Figure** 2b) than the optical data. In **Figure** 2b, the mean square slopes derived from GEOS3 reported in Brown (1990) and shown as crosses are digitized from his **figure** 7. The in-situ wind speeds were compiled from ocean buoys in the vicinity of the satellite footprint at the time of satellite passages. The spatial lag with one standard deviation between the satellite data and surface wind measurements is 30.1 ± 23.2 km, and the temporal lag is 0.56 ± 0.42 hours (Brown, 1981, 1990). The data shown as circles are derived from TOPEX track 115 and NDBC Buoy 42020 (270°00'44"N, 90°30'20"W, local water depth 132m) in the Gulf of Mexico. Only those data points satisfying the stringent criteria of spatial lags less than 10 km and temporal lags less than 0.5 hours are plotted (a total of 208 points). Due to the relatively mild conditions in the Gulf of Mexico, the maximum wind speed encountered in this three-year (1993 to 1995) database is only 11 m/s, considerably less than that of Brown's measurements (1981, 1990).

Overall, these two data sets, separated by approximately two decades, are quite similar and display a trend considerably different from the mean trend of the optical measurements (solid curve). At higher wind speed, say U_{10}> 8 m/s, the linear wind dependence appears to hold. At lower wind speed, the deviation from a linear wind speed relationship is evident. The data scatter is also much more pronounced in the radar measurements, especially at the lowest wind speed range. Most important of all, the radar-derived mean square slopes are obviously higher than the optically-measured values at the same wind condition, a clear violation of the physics of wave scattering as commented earlier.

One common practice to reconcile this difference is to lower the magnitude of $|R(0)|^2$ from the observed value of 0.61 for Ku-band radar frequency (Stogryn, 1971; Ray, 1972; Klein and Swift, 1977). The reason for the reduced coefficient is sometimes attributed to the effects of wave breaking and foamy surface modifying the surface reflective properties. This approach is not justified, especially in view of the fact that major discrepancies of radar and optical data occur under the mild wind condition such that the modification of dielectric constant by foams and breaking is most likely minimal. The trend of the radar-optical discrepancy should be reversed from that shown in **Figure** 2b.

Another explanation for the reduced radar backscattering intensity suggested by Jackson et al. (1992) is due to the diffraction effect from roughness of very short lengthscales. This is also considered by Thompson (1988) and Chapron et al. (1995) among others. They have shown that by carrying out the solution of EM wave scattering from a rough surface to the higher order, the diffraction effect reduces the mean square slopes calculated from radar backscattering cross section. Using the ratio (of the surface wavelength to the radar wavelength) of 3 as the scale of separating the diffraction and scattering roughness components, Jackson et al. (1992) show that the diffraction mechanism can effectively reduce the calculated mean square slopes to less than the optical measurements at higher wind condition (U_{10}>7 m/s). The diffraction mechanism, however, is not effective at lower wind speeds and the mean square slopes derived from radar at wind speeds less than 5 m/s remain higher than the optical values (see **figure** 4 of Jackson et al., 1992). In summary, the correction due to the diffraction mechanism decreases from high wind to low wind conditions. This is an opposite trend to that displayed in **Figure** 2b, where it is illustrated that the major discrepancies between radar and optical measurements occur in the low wind region and that the differences reduce toward higher wind speeds. We therefore conclude that the diffraction effect as formulated is not the major mechanism responsible for the observed discrepancies of radar and optical measurements in the mild to moderate wind speed conditions, say, U_{10} < 8 m/s.

2.3. Tilting effect on the altimeter backscattering

The information embedded in **Figure** 2 can be expressed in a different form as σ_0 vs. U_{10} (**Figure** 3). In **Figure** 3a, the solid curve is calculated using (2) with the optically-derived surface roughness (3) multiplied by a factor of 0.7. More discussion on the computation of the surface roughness components will be presented in the Section 3.4. It becomes clear that the proper interpretation of the "excessive roughness" as shown in **Figure** 2b is really an attenuation factor, $\Delta\sigma_0$, that is more significant under

lower wind than higher wind conditions. This attenuation factor can be calculated from the difference (in dB) of the calculated (the solid curve of **Figure** 3a) and the measured (the circles in **Figure** 3a) radar cross sections. The results are shown in **Figure** 3b. (Note, a difference in dB between the measured and the calculated σ_0 corresponds to the ratio of the two quantities.) As discussed earlier and illustrated in **Figure** 1, the important length scale governing the scattering phenomenon is not the size of the radar footprint but the length scale of surface undulations with respect to the radar wavelength. While small scale roughness with wavelengths comparable to the radar wavelength contributes to the scattering, the primary effect of longer waves is to change the local incidence angle (**Figure** 1) such that the back scattering intensity decays at an exponential rate, due to the $\exp(-\tan^2\theta_i/s_f^2)$ term in (1). This exponential decay is most significant at lower wind speeds, under which the mean square slope, s_f^2, is small, and less severe at higher wind with $s_f^2 >> \tan^2\theta_i$. The trend of this decay due to the local incidence angle variation is in agreement with the wind-dependent attenuation of the radar return shown in **Figure** 3b. It is concluded that the computation of σ_0 needs to take into consideration the local incidence angle variation caused by longer waves on the ocean surface.

sigufit.m

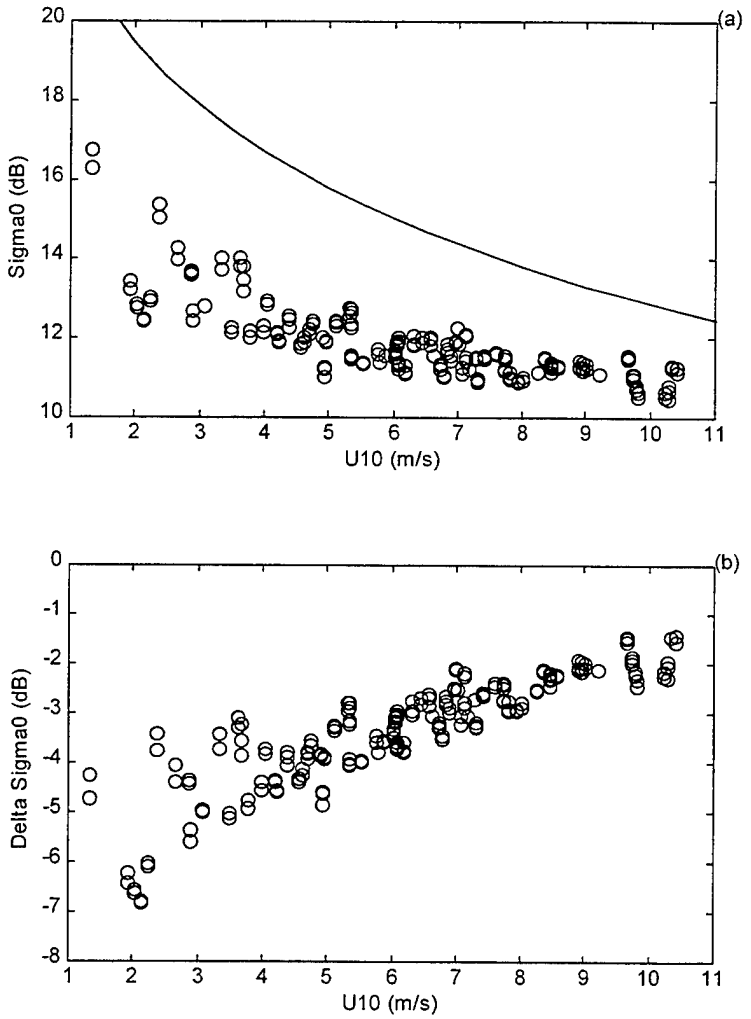

Figure 3. (a) The wind speed dependence of the normalized radar cross section, σ_0; o: TOPEX Ku-band altimeter measurements; and solid curve: calculation by Eq. (2) with s_f^2 defined as 0.7 times the optically-measured mean square slopes (Eq. 3). (b) The damping factor, $\Delta\sigma_0$ (Eq. 6).

Introducing the concept of local incident angle (e.g., Wright, 1968; Valenzuela, 1976), (1) can be expressed as

$$\Sigma_o(\theta_i) = \int \frac{|R(0)|^2}{s_f^2} \sec^4(\theta_i + \theta) \exp\left(\frac{-\tan^2(\theta_i + \theta)}{s_f^2}\right) p(\theta) d\theta \ , \tag{4}$$

where θ is the slope of the long wave roughness (the tilting waves) that contributes to the modification of the local incidence angle, $p(\theta)$ is the probability density distribution (pdf) of the tilting waves, and Σ_0 is the expected radar cross section measured by the altimeter. This modification is most significant at θ_i=0, that is, the altimeter mode. Qualitatively, this can be explained by exploring the exponential term on the right hand side of (4), $\exp(-\tan^2(\theta_i+\theta)/s_f^2)$. One may expect that the relative change of the local incident angle $[(\theta_i+\theta)/\theta_i]$ is most significant as θ_i approaches 0°.

For normal incidence, θ_i=0, and (4) becomes

$$\Sigma_o(0) = \int \frac{|R(0)|^2}{s_f^2} \sec^4\theta \exp\left(\frac{-\tan^2\theta}{s_f^2}\right) p(\theta) d\theta \ . \tag{5}$$

In the following, we shall write $\Sigma_0=\Sigma_0(0)$. The analytical form of the attenuation factor, $\Delta\sigma_0$, is given by the ratio of Σ_0 and σ_0

$$\Delta\sigma_0 = \frac{\Sigma_o(0)}{\sigma_0(0)} = \int \sec^4\theta \exp\left(\frac{-\tan^2\theta}{s_f^2}\right) p(\theta) d\theta \ . \tag{6}$$

In the next section, we present the details of the calculation of radar cross section and attenuation factor based on the above formulation for two pdf functions of the tilting waves. The Gaussian surface distribution is given by

$$p_g(\theta) = \frac{1}{\sqrt{2\pi\sigma_t^2}} \exp\left(\frac{-\theta^2}{2\sigma_t^2}\right) \ , \tag{7}$$

and the sinusoidal surface distribution by

$$p_s(\theta) = \frac{1}{\pi\sqrt{\left(A_t^2 - \theta^2\right)}} \ , \tag{8}$$

where σ_t is the root mean square slope of random tilting waves and A_t is the maximum slope of the representative sinusoidal tilting waves. Both σ_t and A_t will be quantified later.

2.4. An operational algorithm considering the tilting mechanism

Based on the above analysis, an operational algorithm to derive wind speed from altimeter data can be established from the scattering equation (5). To obtain a closed-form solution of the integration in (5), the tilting angle θ is further assumed to be small, resulting in the following simplification

$$\Sigma_o = \int \frac{|R(0)|^2}{s_f^2} \exp\left(\frac{-\theta^2}{s_f^2}\right) p(\theta) d\theta \ . \tag{9}$$

With the Gaussian distribution, (9) becomes

$$\Sigma_o = \frac{|R(0)|^2}{s_f^2}\sqrt{\frac{s_f^2}{s_f^2+2\sigma_t^2}} \quad . \tag{10}$$

Considering that the scattering roughness component, s_f^2, is the wind-generated short waves, while the longer tilting component may contain both wind-generated waves, s_t^2, and ambient waves, S^2, that are not related to local wind speed, we can write $s_f^2=B_1U_{10}$, $\sigma_t^2=s_t^2+S^2$, and $s_t^2=B_2U_{10}+B_3$ (to be further described in the next section), (10) becomes a quadratic equation of U_{10}, with the following positive root,

$$U_{10} = \frac{-K_2+\sqrt{K_2+4K_1K_3}}{2K_1} \quad , \tag{11}$$

where $K_1 = B_1^2+2B_1B_2$, $K_2=2B_1(B_3+S^2)$, and $K_3=(|R(0)|^2/\Sigma_0)^2$. Eq.(11) is an operational algorithm that can be used to derive the wind speed from the altimeter output alone.

3. Numerical Calculation

3.1. Dividing scales of tilting and scattering roughness components

In order to carry out the calculation of (5), one needs to define the scale length and the wavenumber distribution of the surface roughness. In this paper, we use the half-wavelength ($L/2$) of the surface undulation as the characteristic length scale (a) of the surface roughness. This scale corresponds to the characteristic length of the surface "mounds" or "depressions" illustrated in **Figure** 1. The short waves with κa in the range of 1 to 50 will be considered as the filtered roughness, s_f^2, and the components with $\kappa a > 50$ will be considered as the tilting fraction, s_t^2, that contributes to the variation of the local incidence angle. For the Ku-band frequency (13.6 GHz) used on TOPEX, the corresponding wavelengths of tilting and diffraction limits based on the above criteria are 0.35 and 0.007 m; and the corresponding wavenumbers are 18 and 896 rad/m, respectively.

3.2. Wavenumber spectrum of short ocean waves and components of surface roughness

The wavenumber spectrum describing the ocean surface slope, $\chi_1(k)$, is needed to carry out the computation. It is noted that the majority of ocean wave data are from point measurements that provided the frequency spectrum. The functional form of the wave spectrum is still a topic of active research. There is a factor-of-two uncertainty in the measured values of the spectral coefficient in the frequency domain (Phillips, 1985). The conversion from frequency to wavenumber domain is nontrivial and introduces further uncertainties due to the lack of definitive information on the directional distribution of the wavenumber spectrum. Phillips (1977, 1985) presents detailed discussions of the spectral properties in the "saturation" region, the correlation between the frequency spectral coefficient and the wavenumber spectral coefficient, and the difficulties associated with the procedure for the conversion of frequency to wavenumber spectra. These discussions will not be repeated here.

Of special interest for the present computation are the short-scale waves based on the recent field data of capillary-gravity waves. These spatial measurements were acquired by a scanning slope sensor mounted on a free-drifting buoy to reduce flow disturbances to the sensing region (Hwang, 1995, 1997; Hwang et al., 1996). The data cover the wavenumber range of 100 to 1600 rad/m (wavelengths from 0.004 to 0.063 m), corresponding to the region approximately four times shorter to four times longer than the critical wavenumber (k_m) of 374 rad/m, under which the phase velocity of the wave component (c_m) is at a minimum and the contributions of gravity and surface tension as the restoring forces of wave motion are equal. Based on these field data, the following empirical spectral function for the short waves in the ocean is proposed:

$$\chi_1(k) = A(u*/c)(c_m/c)k_m k^{-2}, \tag{12}$$

where A is the dimensionless spectral parameter, $u*$ the wind friction velocity, and c the phase speed.

The wavenumber dependence of the calculated values of the coefficient A from field data is found to be monotonic, with A approaching an asymptotic value of $(2.3\pm0.55)\times10^{-3}$ at the gravity end, and $(2.1\pm0.11)\times10^{-2}$ at the capillary end of the wavenumber range (**Figure** 4). The following three-segment approximation, shown as solid line segments in **Figure** 4, will be used for the subsequent calculation

$$\chi_1(k) = \begin{pmatrix} 2.01\times10^{-2}u*k^{-1}, & k_t < k < 100\,rad/m \\ 1.97\times10^{-3}u*\left(g+\tau k^2\right)^{-1}, & 100 < k < 900\,rad/m \\ 2.57\times10^{4}u*k^{-3}, & 900 < k < 1600\,rad/m \end{pmatrix}, \tag{13}$$

where k_t is the wavenumber (18 rad/m) separating the tilting roughness and filtered scattering roughness, g the gravitational acceleration and τ the ratio of surface tension and water density. Note that the coefficients in (13) are dimensional and MKS units are used.

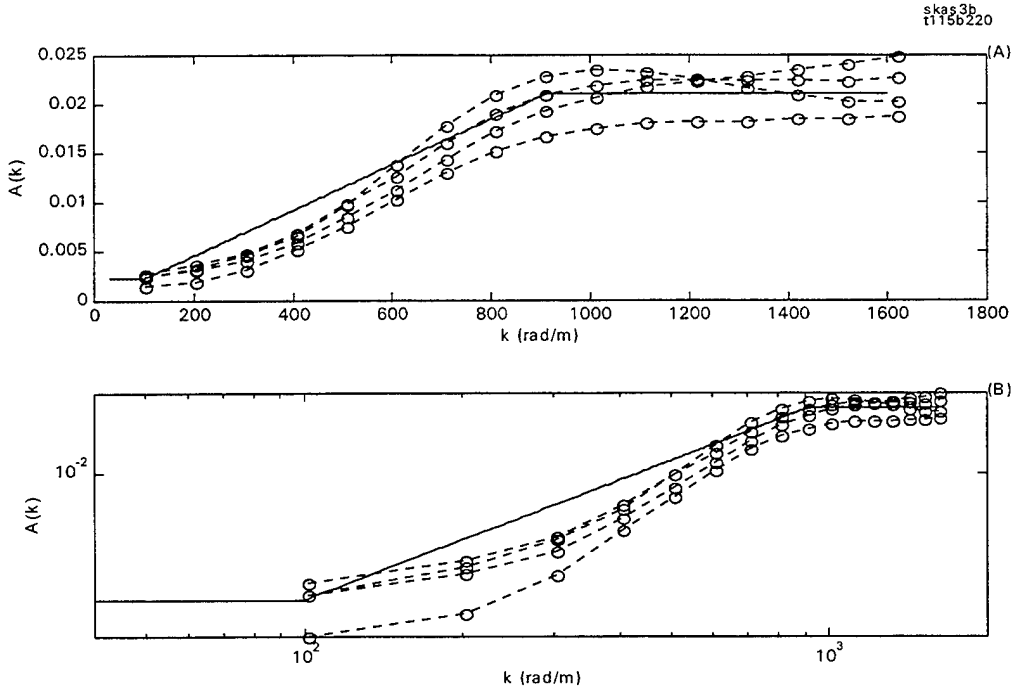

Figure 4. (*a*) The dimensionless spectral coefficient, A, calculated from the measured curvature wavenumber spectra (Hwang et al., 1996, Hwang, 1997), showing the asymptotic trend in the gravity and capillary wave regions. The solid curve is the three-segment approximation (Eq. 14) described in the text. (b) Same as (a) but plotted in linear scale.

The slope spectrum can be expressed in terms of U_{10} instead of $u*$ with the relation $u*=C_D^{1/2}U_{10}$, where C_D is assumed to be a constant 0.0012, a reasonable assumption for mild to moderate wind conditions (Large and Pond, 1987). Thus

$$\chi_1(k) = \begin{pmatrix} 6.96\times10^{-4}U_{10}k^{-1}, & k_t < k < 100\,rad/m \\ 6.82\times10^{-5}U_{10}\left(g+\tau k^2\right)^{-1}, & 100 < k < 900\,rad/m \\ 8.90\times10^{2}U_{10}k^{-3}, & 900 < k < 1600\,rad/m \end{pmatrix}. \tag{14}$$

Integrated (14), the filtered ($18<k<896$ rad/m) and the diffraction-limit ($k>896$ rad/m) roughness components can be expressed explicitly as

$$s_f^2 = 3.66 \times 10^{-3} U_{10} \tag{15}$$

and

$$s_d^2 = 3.74 \times 10^{-4} U_{10}. \tag{16}$$

The wind-induced tilting roughness component ($k<18$ rad/m) can be calculated by subtracting (15) and (16) from (3), which gives

$$s_t^2 = 1.09 \times 10^{-3} U_{10} + 1.25 \times 10^{-3}. \tag{17}$$

As stated in the last section, in addition to the wind-induced roughness, other features, such as swells generated from far away regions, and breaking waves and turbulence at the local ocean surface, will also introduce apparent surface slopes which do not have a clear functional dependence on the local wind speed. Denoting these non-local-wind contributions as S^2 (hereafter referred to as the ambient parameter), the variance of the tilting surfaces in (7) is explicitly,

$$\sigma_t^2 = s_t^2 + S^2, \tag{18}$$

and in (8)

$$A_t^2 = 2\left(s_t^2 + S^2\right). \tag{19}$$

3.3. Ambient parameter

The measurement of mean square slopes in the ocean is a very difficult task, and the separation of wind-induced and ambient components has been only recently attempted (Hwang, 1997). We may, however, estimate the range of the ambient parameter S^2. For a periodic wave train, it has been established that the maximum ratio of wave height to wavelength is 1/7 (Michell, 1893), corresponding to a steepness (defined as the product of the wavenumber and the wave amplitude) of $\pi/7$, The mean square slope of a sinusoidal wave train with maximum slope is then $(\pi/7)^2/2 = 0.10$, representing the maximum value of S^2.

Although NDBC buoys are operational buoys with a cutoff frequency of 0.4 Hz (wavelength 10m), their standard output of the average period, T_a, and the significant wave height, H, may be used for an estimate of the ambient parameter. The buoy-measured mean square slope is calculated by $S_b^2 = (K_a H)^2/8$, where K_a is calculated from T_a, using the deep water dispersion relationship. The attenuation factor, $\Delta\sigma_0$ vs. S_b^2 is shown in **Figure** 5 with different symbols for wind speed bands of U_{10} = [1, 2.5], [2.5 ,4], [4, 5.5], [5.5, 7], [7, 8.5] and [8.5, 11] m/s. The maximum wind speed of the data set is 11 m/s. The strong dependence of $\Delta\sigma_0$ on S_b^2 is clearly illustrated. For the data points in each wind speed band, $\Delta\sigma_0$ decreases by 1 to 2 dB at the higher end of S_b^2. The magnitude of $\Delta\sigma_0$ tends to level off when S_b^2 is small, probably indicating the absence of swells and other ambient waves. In addition, the functional dependence of $\Delta\sigma_0$ as a function of U_{10}, and therefore of s_f^2, is evident in this plot. Such dependence on the long wave steepness and wind speed is expected from the tilting effect as described earlier in Section 2.3.

It is noted that rather large S_b^2 values exist in the lower wind speed data. Values as much as 5.2×10^{-3} are observed with $U_{10} < 3$ m/s. The expected wavelength at the spectral peaks of these low wind cases is less than 6 m, therefore, the wave properties measured by the buoy are predominantly ambient waves that are not locally-generated. At this point, we clarify that the operational buoys are not designed to measure wave slopes. For example, the maximum value of S_b^2 shown in the **Figure** 5 is only 0.013 at U_{10} = 11 m/s, where breaking undoubtedly occurs. As mentioned earlier, the mean square slope

of waves at the breaking limit is 0.1. Studies of breaking waves have shown the difficulties of deriving the mean square wave slopes or the acceleration parameters (both are related to the fourth moments of the wave spectrum) using wave buoys (see, e.g., Snyder et al., 1983; Hwang et al., 1989). It is estimated that S_b^2 may represent an underestimation (by a factor between 5 and 10) of S^2. Even with these reservations, it is quite encouraging to see that the functional dependence of the attenuation factor on the wind speed and large scale surface slopes as displayed in **Figure** 5 is in good agreement with the prediction of the tilting mechanism. Computational results with a reasonable range of S^2 (0 to 0.03) will be presented below.

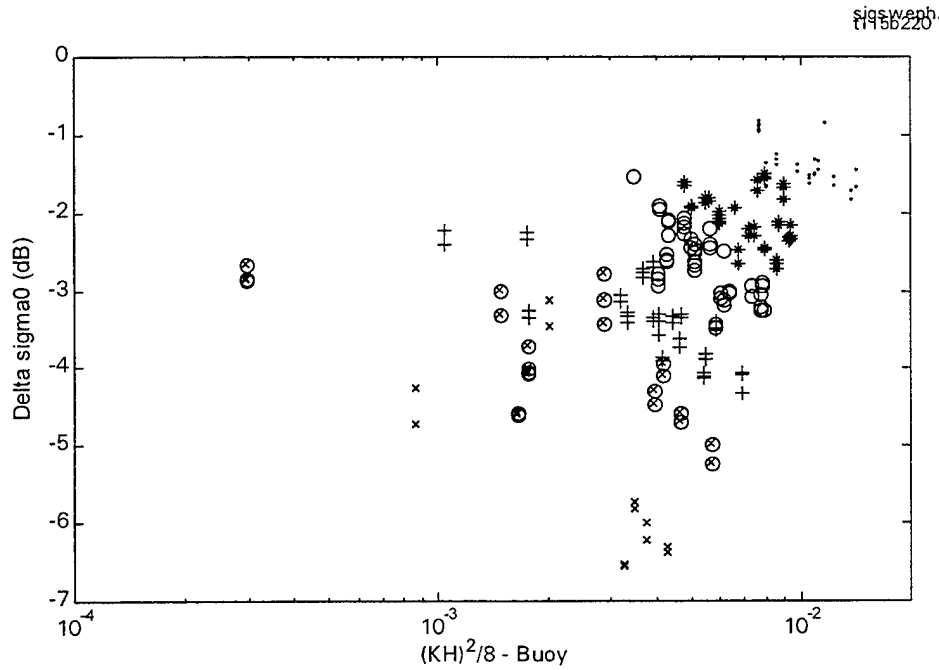

Figure 5. Using the buoy-measured wave slopes ($S_b^2=(KH)^2/8$, calculated from the average period and wave height reported in the buoy data suite) as an indication of the ambient slopes, S^2, the attenuation factor, $\Delta\sigma_0$ for a given wind speed band is shown to decrease with increasing S_b^2, in agreement with the theoretical prediction of the tilting mechanism. Symbols: x: U_{10}=1 to 2.5 m/s, ⊗: U_{10}=2.5 to 4 m/s, o: U_{10}=4 to 5.5 m/s, +: U_{10}= 5.5 to 7 m/s, *: U_{10}= 7 to 8.5 m/s, •: U_{10}>8.5 m/s.

3.4. General properties of the tilting solution

With the tilting and filtered roughness components defined, the dissipation factor, $\Delta\sigma_0$, derived from (5) is shown in **Figure** 6a for the Gaussian distribution, and in **Figure** 6b for the sinusoidal distribution. In both figures, five curves are shown for S^2=0, 5×10^{-3}, 1×10^{-2}, 2×10^{-2} and 3×10^{-2}, from top to bottom, respectively. The numerical integration of (6) is carried out with the integration range of θ from $-4\sigma_t$ to $4\sigma_t$ for the Gaussian distribution of the tilting waves, and from $-A_t$ to A_t for the sinusoidal distribution. It is seen that even without the introduction of the ambient parameter (S^2=0), the attenuation factor ranges from -1dB at U_{10}=11 m/s to -1.8 dB at U_{10}=1 m/s using the Gaussian distribution; and from -1.4 dB to -2.4 dB using the sinusoidal distribution. In terms of ratios, -1, -1.4, -1.8 and -2.4dB correspond to 0.79, 0.72, 0.66 and 0.58 respectively. The tilting effect, therefore, represents a major correction to the altimeter backscattering cross section. A comparison of **Figures** 6a and 6b with 3b suggests that S^2 varies from a range of [0, 0.01] at wind speed above 10 m/s to [0.005, 0.03] at low winds in the 1 m/s range, assuming a Gaussian distribution of the tilting waves. Although a functional form of $S^2(U_{10})$ will undoubtedly improve the agreement between computations and measurements, the fine tuning of the S^2 parameter (as well as the partitioning roughness length scales, k_d and k_t, and the spectral function of the short ocean waves) is not pursued here. Instead, from visual inspection it is considered

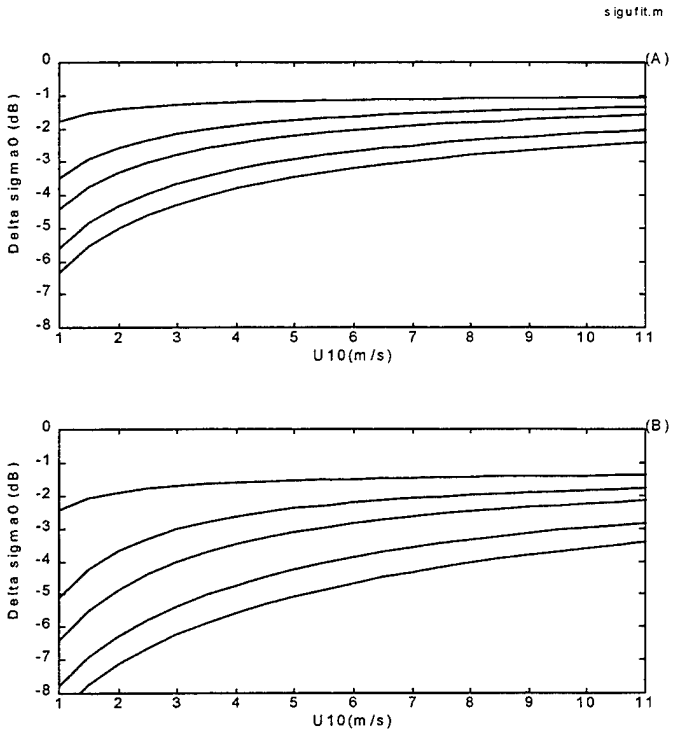

Figure 6. (a) Calculated $\Delta\sigma_0$ using Eq. (6) for S^2=0, 5×10^{-3}, 1×10^{-2}, 2×10^{-2}, and 3×10^{-2} (top to bottom) and a Gaussian surface (Eq. 7); (b) Same as (a) but for a sinusoidal surface (Eq. 8)

4. Comparison With Other Wind Speed Algorithms

4.1. Present status

There have been many comparisons of existing altimeter wind algorithms (e.g., Witter and Chelton, 1991; Wu, 1992; Freilich and Challenor, 1994). Freilich and Challenor (1994) present a very comprehensive analysis of eight algorithms. Results in terms of the mean error, root mean-square error, standard deviation, wind speed error trend, and pseudo-wave age error trend are tabulated. The differences in all eight algorithms are surprisingly minor, especially in terms of the mean square error or standard deviation: 7 of the 8 algorithms produce less than 10 percent differences in these two error parameters (1.60 to 1.75 m/s rms error, 1.58 to 1.72 m/s standard deviation). The corresponding values for the eighth algorithm (NWP3, Freilich and Dunbar, 1993) are slightly higher and close to 2 m/s. It can be concluded that the statistical or empirical approach to develop wind speed algorithms from satellite altimeters may have reached its resolution limit. The approaches of statistical and empirical fitting also do not explain the discrepancy between the optical and radar measurements discussed earlier (**Figure** 2b). The tilting mechanism described in the last section is based on the physical property of wave scattering by roughness of different length scales (relative to the incidence radar wavelength). The apparently "rougher" surface perceived by the radar is clarified to be an indication of signal attenuation due to the modification of the local incidence angle by surface roughness components of longer length scales.

4.2. Effect of surface tilting

Here, we present the comparison of the tilting mechanism as outlined in the previous section, and three other algorithms: Brown [B81] (Brown et al., 1981), Modified Chelton and Wentz [MCW] (Witter and Chelton, 1991), and the Rayleigh-based statistical model [F&C] (Freilich and Challenor, 1994). Two sets of computations will be shown. The first set is a reference calculation using the forward computational procedure [Tilt-Forward] to evaluate (5) with probability distributions (7) and (8). The forward procedure starts with the calculation of the attenuation factor $\Delta\sigma_0$ using (6). The buoy wind

speed (U_{10}(Buoy)) is used to calculate the mean square slope components needed in the equation. The ambient parameter S^2 is fixed at 0.01 for the sinusoidal distribution and 0.02 for the Gaussian distribution. The calculated attenuation factor is then applied to the altimeter measurement of the radar cross section to derive the filtered slopes, sf^2 from (5). The altimeter wind speed, U_{10}(ALT), is then calculated through the linear correlation (15). The purpose of the reference computation is to assess the accuracy of the formulation of the tilting mechanism. The second set of computations is the direct calculation of U_{10}(ALT) using the four operational algorithms just mentioned (B81, MCW, F&C, and Tilt-Operational algorithm (11)). The statistics of comparison include the following: the distribution of the velocity difference ($\Delta U = U_{10}$(ALT) - U_{10}(Buoy)), the root mean square difference, the correlation coefficient, and the slope of the scatter plot (U_{10}(ALT) vs. U_{10}(Buoy)).

The database used in the comparison is from TOPEX Track 115 and NDBC Buoy 42020 in the Gulf of Mexico, covering the period from October 1992 to December 1995 (**Table** 1). Only data points with spatial distance of less than 10 km and temporal difference less than 0.5 hours are used (a total of 208 points). Interestingly, as shown in **Figure** 7a, this data set displays two distinctive branches at low wind conditions (U_{10}<5 m/s). One branch appears to show better agreement with B81 and the other branch shows better agreement with MCW and F&C. The reference calculation (with Gaussian distribution shown) is somewhat closer to the B81 curve at the intermediate wind condition and falls in the middle of the three algorithms in the low wind speed region. The key statistics of comparison, including the rms difference, the correlation coefficient, and the slope of scatter plot (TOPEX wind speed vs. Buoy wind speed) are listed in **Table** 1. With the forward computation, the rms errors are significantly reduced (from an average of 1.28 m/s to 0.82 m/s using the Gaussian surface assumption, and to 0.74 m/s using the sinusoidal surface assumption), and the correlation coefficient of TOPEX wind speeds with buoy wind speeds increases from 0.85 to better than 0.95. **Figure** 7b shows the scatter plot of the buoy measurements and the TOPEX wind speeds derived from the reference calculation of the tilting-surface model. The agreement is considerably better than other existing algorithms (see, e.g. **figure** 6 of Witter and Chelton, 1991; **figure** 2 of Wu, 1992).

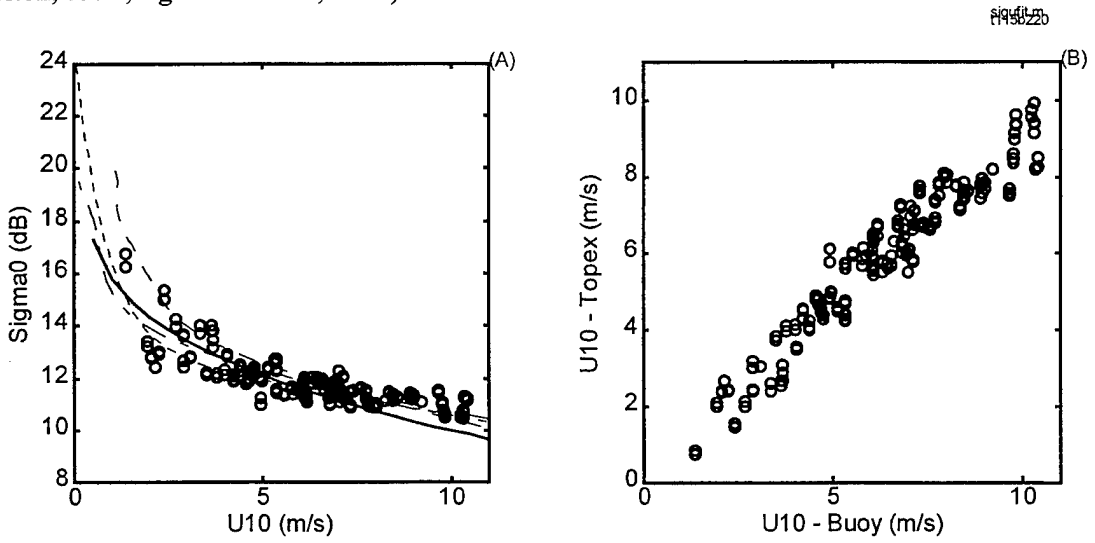

Figure 7. Comparison of different wind speed algorithms. (a)σ_0 vs. U_{10}; circles are TOPEX data; the solid curve is the present tilting-surface model (Eq. 5); the long-dashed is B81 (Brown et al., 1981); the long -short-dashed is MCW (Witter and Chelton, 1991); and the short-dashed is F&C (Freilich and Challenor, 1994). (b) The scatter plot of buoy wind speeds and TOPEX measurements calculated with the present two-scale procedure. Altimeter and buoy data are from Track 115 and NDBC Buoy 42020, a short description of the data set is given in Table 1a.

Figures 8a and 8b show the distributions of ΔU of the forward calculation for the Gaussian and the sinusoidal distributions. The ΔU distributions of B81, MCW, and F&C algorithms are shown in **Figures** 8c to 8e. The last three distributions of ΔU show very similar characteristics, with maximum and minimum differences spread between (-3, 4 m/s), (-2.5, 3.8 m/s), and (-3.6, 3.2 m/s), respectively; and the majority population distributed between ±2 m/s (**Figures** 8c to 8e) . In comparison, the maximum and minimum differences of the reference computation are reduced to -2 to 1 m/s, and the majority population is distributed within the range of -1 to +0.4 m/s (**Figures** 8a and 8b). The distribution of ΔU of the Tilt-Operation algorithm (11) is shown in **Figure** 8f. The distribution resembles more closely to those shown in **Figures** 8c to 8e than those shown in 8a and 8b. The other statistics of comparison listed in **Table** 1 also show a similar resemblance with other empirical algorithms (B81, MCW, and F&C). Comparisons of cases where the distance between satellite footprint and buoy location is larger than 10 km also show similar levels of improvement when the tilting mechanism is included in the forward computational procedure. The statistics of two additional cases [Track 21, Buoy 42020, maximum distance 20 km; Track 46, Buoy 42003, maximum distance 40 km] are also listed in **Table** 1. With the forward computation, the rms difference persistently improves by a factor of approximately 40 percent, with the correlation coefficient greater than 0.9.

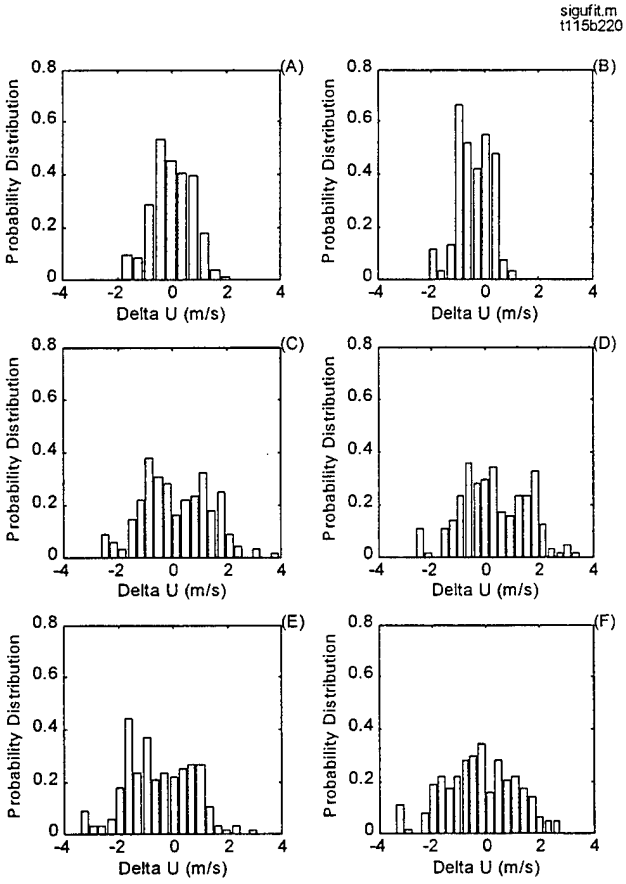

Figure 8. The distribution of the wind speed difference, U_{10}(ALT)-U_{10}(Buoy). (a) and (b) are based on the forward computational procedure (Eq. 5) with, respectively, the Gaussian (Eq. 7) and sinusoidal (Eq. 8) distributions of the tilting surface slopes; (c) to (e) are based on the empirical algorithms of B81, MCW, and F&C, respectively; and (f) is the operational algorithm that includes the tilting mechanism (Eq. 11). Altimeter and buoy data are from Track 115 and NDBC Buoy 42020, respectively. A short description of the data set is given in Table 1a.

4.3. Discussion

Figure 9 summarizes the evolution in time of the comparison statistics of wind algorithms. It is seen that the progress of the algorithm development since 1981 is almost stagnant. The differences among the major operational algorithms are relatively minor (also see the more extensive comparisons described in Freilich and Challenor (1994)). The "stabilized" trend may give the impression that the wind speed resolution of satellite altimeters is approximately 1.3 m/s in regional applications, and 1.7 m/s in global

applications (e.g., Freilich and Challenor, 1994). However, the results presented in **Figure** 8 and **Table** 1 illustrate that the altimeter wind speed resolution is probably significantly better than we have accepted.

Also, the calculated backscattering cross section using the theoretical scattering solution that incorporated the tilting mechanism (5) is in excellent agreement with the altimeter measurements without the need to invoke an unrealistically large surface roughness. This development therefore resolves the long-exited controversy that the mean square slopes measured by radar altimeters to be higher than those measured by optical sensors.

Table 1. Comparison of the tilting formulation with three existing wind speed algorithms.

a) Track 115, Buoy 42020 (27°00'44"N, 96°30'20"W, local mean water depth 131 m): Spatial distance <10 km; Buoy measured wind speed range: 1 to 11 m/s; temporal difference < 0.5 hr.

	RMS Error (m/s)	Correlation Coefficient	Slope
Brown et al., 1981 (B81)	1.27	0.84	1.00
Witter and Chelton, 1991 (MCW)	1.24	0.85	1.00
Freilich and Challenor, 1994 (F&C)	1.33	0.88	0.89
Tilt-Operational, This study (Eq. 11)	**1.31**	**0.84**	**0.96**
Tilt-Forward, Sinusoidal	**0.74**	**0.97**	**0.92**
Tilt-Forward, Gaussian	**0.82**	**0.94**	**0.99**

b) Track 21, Buoy 42020 (27°00'44"N, 96°30'20"W, local mean water depth 131 m): Spatial distance < 20 km; Buoy measured wind speed range: 1 to 13 m/s; Temporal difference < 0.5 hr.

	RMS Error (m/s)	Correlation Coefficient	Slope
Brown et al., 1981 (B81)	1.28	0.91	0.93
Witter and Chelton, 1991 (MCW)	1.23	0.92	0.95
Freilich and Challenor, 1994 (F&C)	1.52	0.92	0.87
Tilt-Forward, Sinusoidal	**0.80**	**0.96**	**0.98**
Tilt-Forward, Gaussian	**0.92**	**0.98**	**0.91**

c) Track 46, Buoy 42003 (25°56'10"N, 85°84'51"W, local mean water depth 3164 m): Spatial distance < 40 km; Buoy measured wind speed range: 1 to 13 m/s; Temporal difference < 0.5 hr

	RMS Error (m/s)	Correlation Coefficient	Slope
Brown et al., 1981 (B81)	1.84	0.79	0.94
Witter and Chelton, 1991 (MCW)	1.76	0.82	0.94
Freilich and Challenor, 1994 (F&C)	1.89	0.83	0.85
Tilt-Forward, Sinusoidal	**1.16**	**0.94**	**0.89**
Tilt-Forward, Gaussian	**1.24**	**0.91**	**0.98**

It is reemphasized that the forward computations (5) is a research algorithm rather than an operational algorithm. Because the procedure as formulated requires *a priori* knowledge of the surface roughness components, results shown in **Figure**s 8a and 8b made use of the buoy-measured surface wind speed. The primary purpose of the comparison presented here is to illustrate that the apparent discrepancies of the surface roughness between radar and optical measurements can be explained with correct physical mechanisms. It also serves to show that if such a correction factor is accounted for, wind speeds measured by satellite altimeters and by ocean buoys agree considerably better than previously reported (**Table** 1). To retrieve the wind speed to the full capability of the altimeter, however, remains a

challenge. The calculation by the operational algorithm (11) considers essentially the same tilting effect relating σ_0 and U_{10}. The differences in the outcome between (11) and (5) obviously are due to the direction of applying the computational procedures. That is, significantly better agreement is found in the procedure that derives the attenuation factor (6) from U_{10}. The correction factor accounted for the large difference between the measured and predicted backscattering cross section (**Figure** 3). On the other hand, the procedures that calculate TOPEX wind speed from σ_0 do not produce such a high level of agreement between altimeter and buoy measurements. Our attempts to derive the attenuation correction ($\Delta\sigma_0$) from altimeter output (through iteration, for example) did not produce further improvement of wind speed retrieval from satellite data (in comparison with existing empirical formulae). This is partly due to the fact that the monotonic wind-speed dependence of the attenuation parameter (**Figure** 10a) cannot be reproduced using the altimeter output alone. An example is shown for $\Delta\sigma_0$ vs. σ_0 in **Figure** 10b. We also tried to correlate the residual of the radar cross section (calculated by subtracting the measured radar cross sections, σ_0, from their best-fit wind dependence values) with significant wave heights, H, and pseudo wave age $U_{10}^2/(gH)$ (Glazman and Greysukh, 1993). The improvement in agreement with surface wind measurements is in the third decimal point of the correlation coefficient (for example, the correlation coefficient increases from 0.866 to 0.868 for the data set of Track 115 and Buoy 42020 and the rms decreases from 1.17 to 1.13 m). These improvements are considered insignificant, and the details of these attempts will not be reported here.

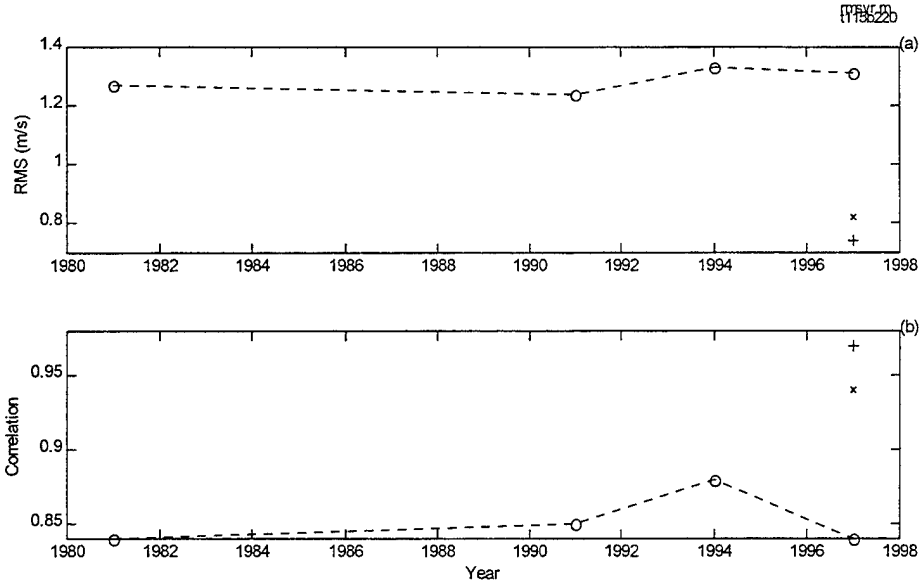

Figure 9. A summary of the comparison statistics of wind speed algorithms developed since 1981, in terms of (a) the rms difference, and (b) the correlation coefficient. The results from operational algorithms (Table 1) are shown as 'o', the forward computational results of the tilting mechanism is shown as 'x' (Gaussian) and '+' (sinusoidal).

5. Conclusions

Wind generates ocean surface waves, which serve as the roughness elements to scatter the impinging radar waves. Thus the measured radar return can be used to derive wind speed. Algorithms to retrieve wind information from satellite altimeters have been under continuous development, with efforts commencing prior to the launch of SEASAT in 1978. During this period of almost two decades, the uncertainty of measurements remained at a level of 1.7 to 2 m/s, and most algorithms were either purely empirically-based or constructed on statistical grounds.

One reason for the lack of progress can be attributed to our poor understanding of the surface roughness characteristics, especially the wavenumber structure needed for the accurate determination of the filtered mean square slopes of a given radar frequency. Another reason is the failure to recognize that the contribution of long-scale (relative to the radar wavelength) surface roughness is mainly to modify the local incidence angle, which produces an exponential attenuation of the altimeter return (see Equations (1) and (4)). This is especially surprising because the two-scale model that takes into account the modification of local incident angle had provided a major improvement in explaining the radar return from moderate and low grazing angles (e.g. Wright, 1966, 1968).

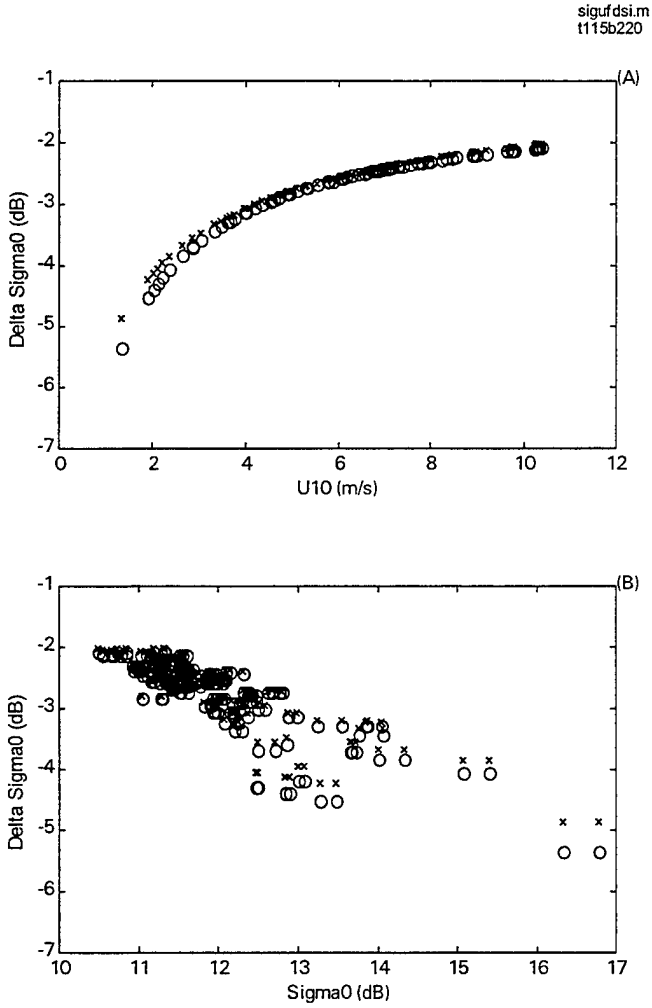

Figure 10. (a) Calculated attenuation factor of the altimeter backscatter cross section, $\Delta\sigma_0$, as a function of wind speed; o: sinusoidal distribution with S^2=0.01, ×: Gaussian distribution with S^2=0.02. (b) Same as (a) but plotted against the radar cross section. Altimeter and buoy data are from Track 115 and NDBC Buoy 42020, respectively. A short description of the data set is given in Table 1a.

The recent in-situ ocean measurements of the short-wave wavenumber spectrum allow a reliable calculation of the mean square slopes of short waves that contribute to scattering, and of the longer waves that contribute to the modification of the local incidence angle. The resulting calculation is consistent with the observed level of signal attenuation of satellite altimeters. Also, it is recognized that turbulence processes and swells may introduce apparent slopes that are not correlated directly to the local wind speed. With these considerations, it is found that the wind speeds measured from altimetry are in much better agreement with in-situ measurements than previously perceived (**Table** 1 and **Figure** 8). This development is very important as it is shown that the accuracy of satellites wind sensing is comparable to that of the in-situ measurement, but it remains a challenge to retrieve the wind speed at its full potential accuracy from altimeter output alone. From the analysis presented earlier, it is suggested that major breakthrough will depend on the capability to derive the ambient and tilting wave slope components from the altimeter data suite. This investigation is in progress.

Acknowledgments We appreciate the stimulating discussions with Ed Walsh and Doug Vandemark of NASA/GSFC. The investigation of the S^2 parameter using the buoy measurements was suggested by David Cotton. This work is sponsored by the Office of Naval Research, Contract N0001496WX30445 (NRL JO-73-7075-06); the Naval Research Laboratory, Job Orders 73-6800-06 and 73-7046-06; and National Data Buoy Center, Contract XA2310501. The research is possible because of the admirable policies of the TOPEX/POSEIDON project to provide the satellite data suite to the public in a timely fashion and the accessibility of the NDBC buoy data.

References

Barrick, D. E., 1968. "Rough surface scattering based on the specular point theory," IEEE *Trans. Antenna. Propag.*, AP-16, 449-454.

Beckmann, P., and A. Spizzichino, 1963. *The scattering of electromagnetic waves from rough surfaces*, Pergamon Press, New York, 503 pp.

Brown, G. S. , 1978. "Backscattering from a Gaussian distributed, perfectly conducting, rough surface," IEEE *Trans. Anten. Propag.*, AP-26, 472-482.

Brown, G. S. , 1981. "The wind speed measurement capability of spaceborne radar altimeters," IEEE *J. Oceanic Eng.*, OE-6, 59-63.

Brown, G. S. , 1990. "Quasi-specular scattering from the air-sea interface," in *Surface Waves and Fluxes, Vol. 2*, eds. W. Plant and G. Geernaert, 1-40, Kluwer Academic.

Brown, G. S., H. R. Stanley, and N. A. Roy, 1981. "The wind speed measurement capability of spaceborne radar altimeters," IEEE *J. Oceanic Eng.*, OE-6, 59-63.

Chapron, B., K. Katsaros, T. Elfouhaily, and D. Vandemark, 1995. "A note on relationships between sea surface roughness and altimeter backscatter," in *Air-Sea Gas Transfer - 3rd International Symposium on Air-Water Gas Transfer*, eds. B. Jahne and E. C. Monahan, Aeon Verlag & Studio, Hanau, Germany, 869-878.

Chelton, D. B. and F. J. Wentz, 1986. "Further development of an improved altimeter wind speed algorithm," *J. Geophys. Res.*, 91, 14250-14260.

Chelton, D. B., E. J. Walsh, and J. L. McArther, 1989. "Pulse compression and sea level tracking in satellite altimeters," *J. Atm. and Oceanic Tech.*, 6, 407-438.

Cox, C. S., and W. Munk, 1954. "Statistics of the sea surface derived from sun glitter," *J. Mar. Res.*, 13, 198-227.

Ebuchi, N., and H. Kawamura, 1994. "Validation of wind speeds and significant wave heights observed by the TOPEX altimeter around Japan," *J. Oceanography,* 50, 479-487.

Fock, V. A. 1965. *Electromagnetic diffraction and propagation problems,* Pergamon Press, New York, 414pp,.

Freilich, M.H., and P.G. Challenor, 1994. "A new approach for determining fully empirical altimeter wind speed model functions," *J. Geophys. Res.*, 99, 25051-25062.

Freilich, M. and H., R.. Dunbar, 1993. "Derivation of satellite wind model functions using operational surface wind analyses: An altimeter example," *J. Geophys. Res.*, 98, 14633-14649.

Fu, L.-L, E.J. Christensen, and C.A. Yamarone, 1994. "TOPEX/POSEIDON mission overview," *J. Geophys. Res.*, 99, 24369-24381.

Glazman, R. E., and A. Greysukh, 1993. "Satellite altimeter measurements of surface wind," *J. Geophys. Res.*, 98, 2475-2483.

Gower, J.F.R. , 1996 "Intercalibration of wave and wind data from TOPEX/POSEIDON and moored buoy off the west coast of Canada," *J. Geophys. Res.*, 101, 3817-3829.

Hughes, B. A., H.L. Grant, and R.W. Chappell, 1978. "A fast response surface-wave slope meter and measured wind-wave moment," *Deep-Sea Res.*, 24, 1211-1223.

Hwang, P.A. , 1995. "Spatial measurements of small-scale ocean waves," in *Air-Sea Gas Transfer - 3rd International Symposium on Air-Water Gas Transfer*, eds. B. Jahne and E. C. Monahan, Aeon Verlag & Studio, Hanau, Germany, 153-164.

Hwang, P. A. 1997. "A study of the wavenumber spectra of short water waves in the ocean. Part 2. Spectral model and mean square slope," *J. Atm. And Oceanic Tech.*, **14**, 1174-1186.

Hwang, P. A., and O. H. Shemdin, 1988. "The dependence of sea surface slope on atmospheric stability and swell conditions," *J. Geophys. Res.*, **93**, 13903-13912.

Hwang, P. A., Xu, D., and Wu, J. , 1989. "Breaking of wind-generated waves: Measurements and characteristics," *J. Fluid Mech.*, **202**, 177-200.

Hwang, P. A., S. Atakturk, M. A. Sletten, and D. B. Trizna, 1996. "A study of the wavenumber spectra of short water waves in the ocean," *J. Phys. Oceanogr.*, 26, 1266-1285.

Jackson, F.C., W.T. Walton, and D. E. Hines, 1992. "Sea surface mean square slope from Ku-band backscatter data," *J. Geophys. Res.*, **97**, 11411-11427.

Kerr, D. E. , 1981. *Propagation of Short Radio Waves*, Peninsula Publ., 728 pp.

Klein, L. A. and C. T. Swift, 1977. "An improved model for the dielectric constant of sea water at microwave frequencies," IEEE *J. Oceanic Eng.*, **OE-2**, 104-111.

Large, W.G. and S. Pond, 1987. "Open ocean momentum flux measurements in moderate to strong winds," *J. Phys. Oceanogr.*, **11**, 324-336.

Michell, J. H. , 1893. "The highest wave in water," *Phil. Mag.*, **36**, 430-437.

Phillips, O. M. , 1977. *The dynamics of the upper ocean*, 2nd ed., Cambridge University Press, 336 pp.

Phillips, O. M. , 1985. "Spectral and statistical properties of the equilibrium range in wind-generated gravity waves," *J. Fluid Mech.*, 156, 505-531.

Ray, P. S. , 1972. "Broadband complex refractive indices of ice and water," *Appl. Opt.*, **11**, 1836-1844.

Stewart, R.H. , 1985. *Methods of Satellite Oceanography*, University of California Press, 360pp.

Snyder, R. L., L. Smith, and R. M. Kennedy, 1983. "On the formulation of whitecaps by a threshold mechanism. Part III: Field experiment and comparison with theory," *.J. Phys. Oceanogr.*, **13**, 1505-1518

Stogryn, A. , 1971. "Equations for calculating the dielectric constant of saline water," IEEE *Trans. Microwave Theory and Tech.*, **MTT-19**, 733-736.

Tang, S., and O. H. Shemdin, 1983.. "Measurements of high frequency waves using a wave follower," *J. Geophys. Res.*, **88**, 9832-9840.

Thompson, D. R., 1988."Calculation of radar backscatter modulations from internal waves," *J. Geophys. Res.*, **93**, 12371-12389.

Valenzuela, G.R. , 1978. "Theories for the interaction of electromagnetic and oceanic waves - a review," *Bound.-Layer Meteorol.*, **13**, 61-85.

Van de Hulst, H. C. , 1987. *Light Scattering by Small Particles*, Dover Publ., 470pp.

Witter, D.L., and D.B. Chelton, 1991. "A Geosat altimeter wind speed algorithm and a method for altimeter wind speed algorithm development," *J. Geophys. Res.*, **96**, 8853-8860.

Wright, J.W. , 1966. "Backscattering from capillary waves with application to sea clutter," IEEE *Trans. Anten. Propag.*, **AP-14**, 749-754.

Wright, J.W., A new model for sea clutter, IEEE *Trans. Anten. Propag.*, **AP-16**, 217-223, 1968.

Wu, J. , 1992. "Near-nadir microwave specular returns from the sea surface - altimeter algorithms for wind and wind stress," *J. Atm Oceanic Tech.*, **9**, 659-667.